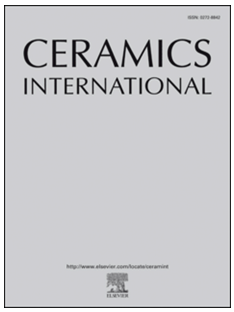

Enhanced electromagnetic microwave absorption properties of SiCN(Fe) ceramics produced by additive manufacturing via in-situ reaction of ferrocene

Yurun Feng, Xue Guo, Hamada Elsayed, Kai Huang, Giorgia Franchin, Guenter Motz, Yanchun Tong, Hongyu Gong, Paolo Colombo

PII: S0272-8842(23)01282-8

DOI: https://doi.org/10.1016/j.ceramint.2023.05.035

Reference: CERI 36564

To appear in: *Ceramics International*

Received Date: 13 January 2023

Revised Date: 17 April 2023

Accepted Date: 4 May 2023

Please cite this article as: Y. Feng, X. Guo, H. Elsayed, K. Huang, G. Franchin, G. Motz, Y. Tong, H. Gong, P. Colombo, Enhanced electromagnetic microwave absorption properties of SiCN(Fe) ceramics produced by additive manufacturing via in-situ reaction of ferrocene, *Ceramics International* (2023), doi: https://doi.org/10.1016/j.ceramint.2023.05.035.

Enhanced electromagnetic microwave absorption properties of SiCN(Fe) ceramics produced by additive manufacturing via in-situ reaction of ferrocene

Yurun Feng [a, b, c,1], Xue Guo [a,1], Hamada Elsayed [b,d], Kai Huang [b], Giorgia Franchin [b], Guenter Motz [e], Yanchun Tong [a], Hongyu Gong [c*], Paolo Colombo [b,f**]

[a] *School of Materials Science and Engineering, Shandong University of Technology, Zibo 255049, China*

[b] *Department of Industrial Engineering, University of Padova, Italy*

[c] *Key Laboratory of Special Functional Aggregated Materials, Ministry of Education, Shandong University, Jinan, 250061, PR China*

[d] *Refractories, Ceramics and Building Materials Department, National Research Centre, El-Bohous Str., 12622 Dokki, Cairo, Egypt*

[e] *Department of Ceramic Materials Engineering, University of Bayreuth, 95447 Bayreuth, Germany*

[f] *Department of Materials Science and Engineering, The Pennsylvania State University, USA*

Abstract

SiCN(Fe) ceramics with excellent electromagnetic wave (EMW) absorption performance were successfully prepared from a preceramic polymer doped with ferrocene. Additive manufacturing (Digital Light Processing), providing enhanced structural design ability, was employed to fabricate samples with complex architectures. During pyrolysis, ferrocene

* Corresponding author at: Key Laboratory for liquid-solid Structural Evolution & Processing of Materials of Ministry of Education, Shandong University, Jinan, 250061, PR China.
** Corresponding author at: Department of Industrial Engineering, University of Padova, Italy.
E-mail addresses: gong_hongyu@163.com (H. Gong), paolo.colombo@unipd.it (P. Colombo).
[1] These authors contributed equally to this work.

catalyzed the in-situ formation of a large amount of turbostratic carbon, graphite and SiC nanosized phases, which formed carrier channels in the electromagnetic field and increased the conductivity loss. Meanwhile, it also increased the dipole polarization, interface polarization and the dielectric properties of the material, which finally enhanced the EMW absorption capacity of SiCN(Fe) ceramics. When containing 0.5 wt% ferrocene, the material showed good performance with EAB 4.57 GHz at 1.30 mm, and RL_{min} -61.34 dB at 2.22 mm. The RL_{min} of 3D-SiCN-0.5 ceramics was -6 dB, and the RL of the X-band was lower than -4 dB at 2 mm.

Keywords: Polymer Derived Ceramics; EMW absorption; SiCN; additive manufacturing.

1. Introduction

With the development of the EMW field, higher structural requirements are required for electromagnetic wave absorbing devices with specific functions. Therefore, 3D printing technology (additive manufacturing) is an effective solution to obtain the integration of structure and function, which will be the focus of the development of EMW absorbing materials in the future[1-3]. Indeed, in recent years, additive manufacturing (AM) has been gradually applied to the design and preparation of absorbing materials. The combination of 3D printing technology and EMW absorbing materials provides a novel concept for the preparation of components with excellent EMW absorbing properties and complex structures, and recently several studies have started to exploit this innovative approach [4-16].

Generally, polymer derived ceramics (PDCs) are obtained from preceramic polymer precursors by heat treatment in inert atmosphere. Based on this characteristic, researchers have

used different AM technologies to fabricate polymer-derived ceramic parts with complex structures [17]. In our previous study, polysiloxane (PSO) was used as main raw material to prepare DLP-SiOC ceramic with log pile or helical icosahedron structure, which showed excellent EMW absorption performance and structural stability [18]. Among PDCs, SiCN ceramics show good development potential in the field of EMW absorption properties due to its good dielectric properties and impedance matching characteristics [19,20]. In addition, the functionalization of the polysilazane (PSZ) precursor by a magnetic component can significantly enhance the EMW absorption properties of PDCs-SiCN ceramics [21-26]. In fact, the in-situ generation of EMW absorbing nanoscale phases (C and SiC phases, Fe containing particles) within the internal structure of the ceramic, during pyrolysis, significantly contribute to the improvement of the EMW absorption performance of the material. Furthermore, the formation of magnetic active nanoparticles effectively improves the impedance matching characteristics of the material, which is also conducive to the improvement of the overall EMW absorption performance [27-29].

Therefore, we manufactured SiCN ceramics with complex structures by digital light processing using ferrocene as modifier, aiming at obtaining an EMW absorption component integrating structure and function.

2. Experimental

Polysilazane (PSZ) powder was obtained by partial cross-linking of commercially available oligosilazane (Durazane 1800 (Merck, Germany)). The oligosilazane was partially crosslinked to a polysilazane (PSZ) following the procedure described by Flores et al [30] leading to a meltable and soluble, in different aprotic solvents, solid. This procedure was carried out for

several reasons: 1) to reduce the chances of introducing some oxygen contamination via reaction with ambient humidity when processing in ambient atmosphere (taking into account the relatively long printing time); 2) to enable a better shape retention during pyrolysis.

In our experiments, the polysilazane powder was dissolved in isopropanol, and a photosensitive polymer (Standard Blend 3D, Fun-to-do, The Netherlands, already containing the photocatalyst) was added together with ferrocene which acted, at the 3D printing stage, as a light absorber to obtain well defined structures in the z-axis direction. The materials were stirred at 60 ºC for 1 h, in polysilazane/solvent/photopolymer weight ratio of 3/3/0.08, while ferrocene (Fluka, 98%, Germany) was added in the amount of 0.5, 1 and 1.5 wt% with respect to the amount of polysilazane. Ferrocene was not added in higher amounts due to its absorption in the wavelength region of the light source, which would have led to much increased exposure time per layer during printing. The obtained solutions were homogenized overnight at room temperature, wrapped in aluminum foil to avoid exposure to light.

The obtained solutions were printed using a DLP printer (3DLPrinter-HD 2.0+, Robofactory, Italy) with a light engine operating with radiation in range of 400-500 nm, using a layer thickness of 0.05 mm and exposure time of 6 s. The printed samples were washed in an ultrasonic bath with isopropanol for 15 min to remove the residual unpolymerized acrylate and then further cured in an ultraviolet furnace (365 nm radiation) for 15 min to complete the formation of the acrylic network. A diamond and a triply periodic minimal surface (gyroid) structure were selected as examples of complex architectures suitable for EMW absorbing components, because of the regularity of the designs and the presence of several surfaces contributing to the reflection and scattering of the impinging EM radiation. The diamond

structure had a size of 10×10×10 mm^3 and the gyroid structure had a size of 35×15×8 mm^3.

The printed samples were pyrolyzed at 1200 ºC for 2 h at heating rate of 1 ºC/min in a tubular furnace under N_2 (99.99%) atmosphere, enabling the formation of different amounts of carbon and β-SiC nanosized clusters catalyzed by the presence of iron compounds. Samples containing 0.0, 0.5, 1.0 and 1.5 wt % ferrocene were labeled SCN-0, SCN-0.5, SCN-1, and SCN-1.5, respectively. Fig. 1 reports the flow chart for the manufacturing of the SiCN(Fe) ceramics.

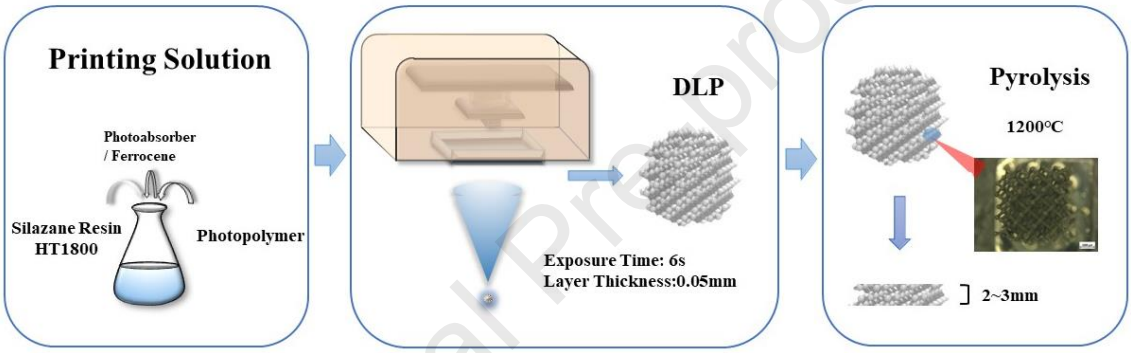

Fig. 1. Schematic representation of the preparation process of the SiCN(Fe) ceramics.

The samples were analyzed by scanning electron microscopy (SEM, JSM-6610LV, Japan), transmission electron microscopy (TEM, JEM-F200 CF-UHR, Japan), X-ray diffractometry (XRD, EVO-18, Carl Zeiss SMT Ltd, Japan), X-Ray Photoelectron Spectroscopy (XPS, PHI1600EXCA, Japan) and Raman (Lab Ram-1 B, France).

First, we tested the performance of the developed material itself, by crushing 3D printed samples into fine powder and mixing it (30 wt%) with paraffin wax and pressing into concentric annular specimens (inner diameter 3 mm, outer diameter mm) with a thickness of 2.50 mm. Then, we proceeded to investigate the electromagnetic absorption performance of a 3D printed SiCN ceramic with a gyroid structure, with or without ferrocene (samples labelled 3D-SiCN-0

and 3D-SiCN-0.5 or 3D-SiCN-1, respectively); the samples 3D-SiCN-0.5 and 3D-SiCN-1 contained 0.5 and 1 wt% of ferrocene, respectively). The electromagnetic parameters were measured by the waveguide short-circuit method (for the analysis, the samples were cut to a 22.76 ×10.06 ×2 mm^3 size). The EMW absorption properties of both powder and 3D printed samples were measured by a vector network analyzer (E5244A, Agilent, USA). The 3D printed samples with a diamond structure were not tested directly, since their size was not adequate for the analytical technique employed.

3. Results and discussion

First of all, we investigated whether the proposed approach (blending pre-crosslinked, soluble silazane with fully organic, sacrificial photopolymer) was adequate for 3D printing complex SiCN structures. Therefore, we proceeded to fabricate samples with a diamond morphology which has a 3D architecture that poses several challenges for its manufacturing (e.g. thin, strongly inclined struts). Considering the shrinkage of the sample during pyrolysis, a diamond structure with 1.5 mm mesh spacing was designed.

Fig. 2 (a) shows the printed polymeric precursor, possessing a regular cubic diamond structure without obvious deformation and defects. Fig. 2 (b) shows the image of a SiCN(Fe) ceramic sample obtained after pyrolysis at 1200ºC. As it can be seen, the diamond structure was fully retained, with no sign of bloating or softening, indicating that the photopolymer present within the structure of the printed sample helped maintaining the geometry of the part at least until the thermal crosslinking of the silazane was achieved during pyrolysis. According to the image of the internal structure (Fig. 2 (c)), the SiCN(Fe) ceramics maintained a well defined

geometric shape throughout the thickness of the sample, after pyrolysis. Considering that no reaction occurs between the acrylate photopolymer and the silazane during 3D printing, the use of partially-crosslinked silazane enables rapid completion of the cross-linking reactions during the initial stages of the pyrolysis, leading to an infusible solid which then retains its shape accurately upon heating. At the same time, no macroscopic pores or defects were visible (Fig. 2 (d)), indicating that the gases deriving from the decomposition of the organic photopolymer and the pyrolysis of the preceramic polymer were able to find suitable pathways for diffusion within the material. The approximate linear shrinkage of the samples after pyrolysis was about 30%. Therefore, we can state that the proposed fabrication method is suitable for fabricating complex porous ceramic structures.

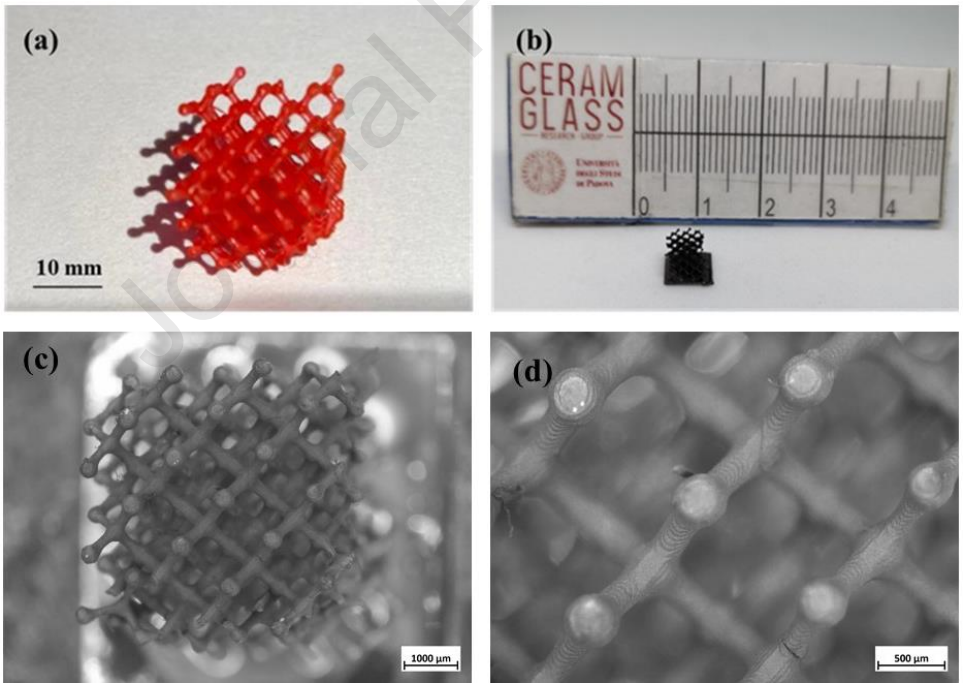

Fig. 2. Optical and stereomicroscopy images of printed samples at different magnifications, before and after pyrolysis. (a) Before pyrolysis; (b) after pyrolysis; (c) stereomicroscope image of whole structure; (d) local enlarged stereomicroscope image.

The microstructural development of the SiCN material containing different amounts of ferrocene during pyrolysis was investigated. Fig. 3 (a) shows the TGA curve of the different photocurable systems developed, together with that of the individual constituents. The photocurable resin (FTD) started to gradually decompose from the beginning of the pyrolysis process, but the major weight loss occurred only above ~300°C, confirming that its presence contributed providing stability to the entire printed structure supporting the un-crosslinked silazane until the onset of thermal crosslinking (see the small weight loss occurring at ~200°C for the pure PSZ), followed by its polymer-to-ceramic transformation in the ~400-800°C temperature range. The thermogravimetric data of the PSZ/FTD mixtures was consistent with the behavior of each individual component. Meanwhile, the introduction of ferrocene had little effect on the final weight loss of the photocurable solutions. According to the XRD results (Fig. 3 (b)), the SiCN(Fe) ceramics pyrolyzed at 1200ºC with different contents of ferrocene mainly contained graphite, turbostratic carbon and β-SiC (micro-)crystalline phases. With increasing amount of ferrocene, the crystallization degree of graphite gradually increased (as proven also by the Raman data). In addition, the crystallization degree of β-SiC appeared to first increase and then decrease with increasing content of ferrocene [31].

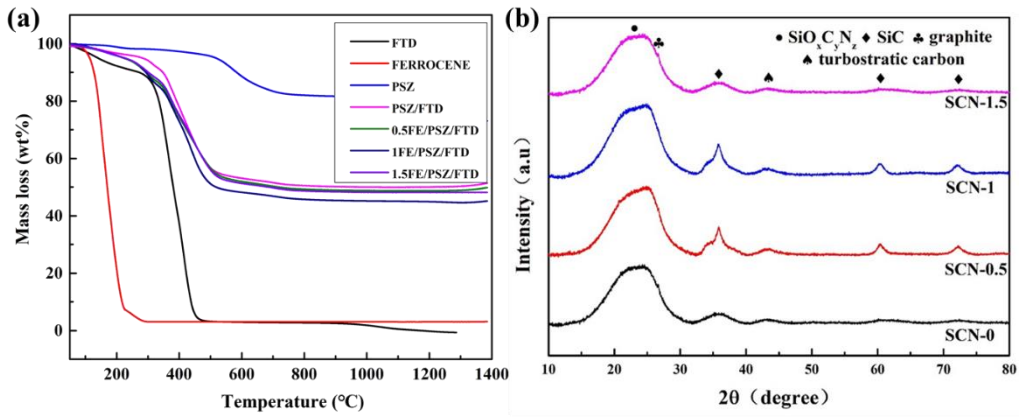

Fig. 3. (a) TGA curves of the different photocurable solutions and of the individual

components; (b) XRD patterns of the SiCN(Fe) ceramics with different ferrocene content.

Fig. 4 shows the TEM images of the samples prepared with different content of ferrocene. The results show that the SiCN(Fe) ceramics were mainly amorphous, accompanied by a small amount of crystalline phases. As shown in Fig. 4 (a), SCN-0 was mainly amorphous with a certain amount of turbostratic carbon [32]. With the introduction of ferrocene, nano-phases including crystalline graphite and β-SiC clusters gradually precipitated in the sample. In addition, the polycrystalline diffraction pattern of SiC can be clearly observed in Fig. 4 (b) and (c). With increasing amount of ferrocene, the crystallinity degree of graphite and the separation of the SiC phase increased significantly, with the SiC particles gradually nucleating and growing. Moreover, the crystallization degree of SiC in the samples (Fig. 4 (d)) decreased with the addition of ferrocene (1.5 wt %), which is due to the simultaneous precipitation of graphite as SiC crystals were competing in the nucleation and growth process. Therefore, increasing the content of ferrocene appeared to favor the growth of graphite crystals, accordingly affecting also the nucleation and growth of SiC particles [32-34].

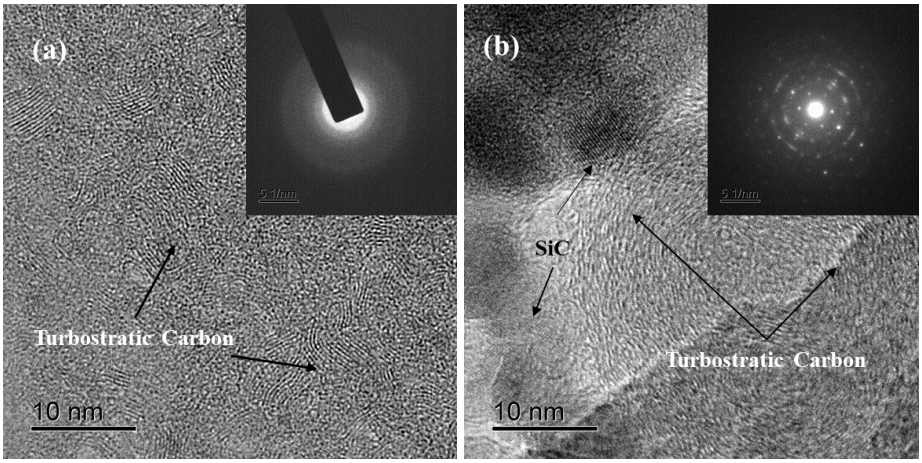

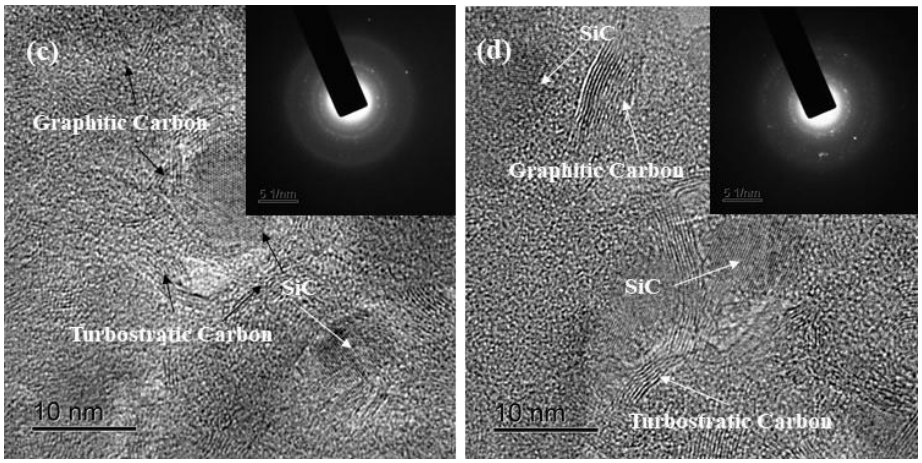

Fig. 4. TEM images of the SiCN(Fe) ceramics with different content of ferrocene. (a) SCN-0; (b) SCN-0.5; (c) SCN-1; (d) SCN-1.5.

The SEM images of the fracture surface of the SiCN(Fe) samples prepared with different content of ferrocene are shown in Fig. 5. No significant features could be observed, due to the mainly amorphous nature of the material, with no obvious pores or cracks at the micro scale indicating that the removal of photosensitive resin phase did not produce defects. The microstructure at this dimensional scale appeared more uniform than that of PDCs prepared by directly converting the polymer into a ceramic [35], possibly due to the presence of the decomposing organic photopolymer generating interconnected pathways for the release of pyrolysis gases during heating.

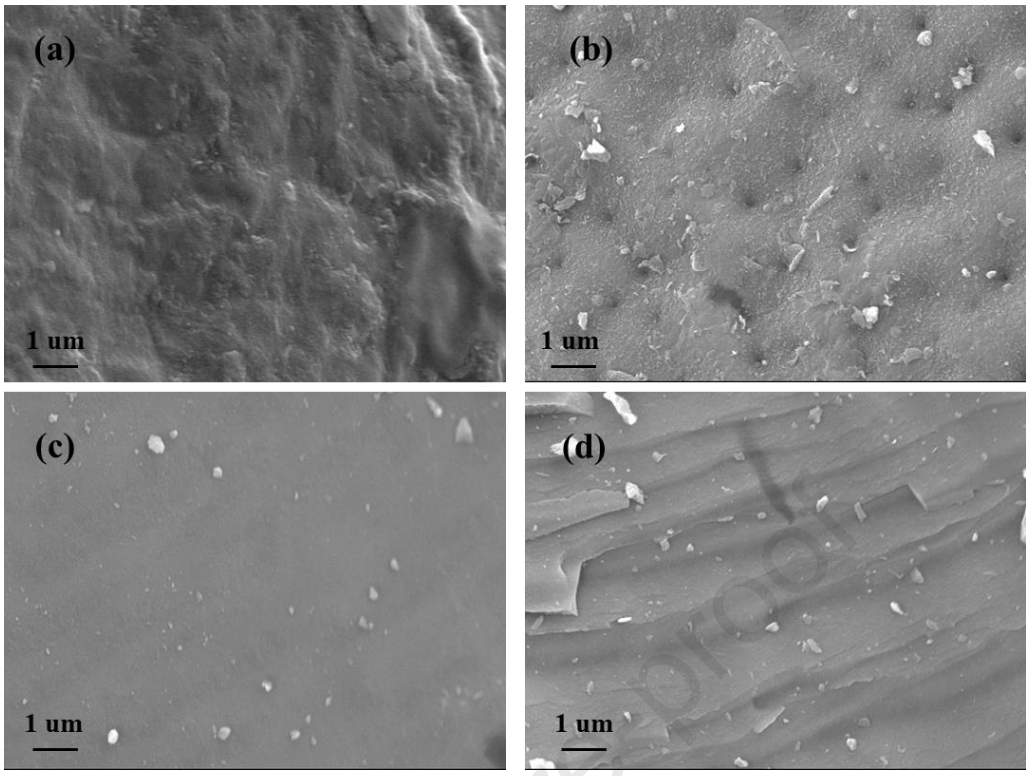

Fig. 5. SEM images of the fracture surface of the SiCN(Fe) ceramics.

(a) SCN-0; (b) SCN-0.5; (c) SCN-1; (d) SCN-1.5

Fig. 6 shows the XPS spectra and fitting curves of SiCN(Fe) samples with different contents of ferrocene. According to Fig. 6 (a), the ceramics were mainly composed of Si, C, N and O elements, as expected. The presence of Fe was observable only for the sample containing the largest amount of ferrocene (SCN-1.5). In order to analyze the chemical bonds present in the samples, peak separation fitting was carried out for Si 2P, C 1s, N 1s and O 1s spectra. As shown in Fig. 6 (b), the Si 2P spectrum was mainly composed of Si-N, Si-O and Si-C bonds, and the content of Si-C bonds gradually increased with increasing content of ferrocene. The results demonstrated that the introduction of ferrocene promoted the precipitation of graphitic carbon and the formation of β-SiC, which had a significant effect on the EMW absorption performance of the SiCN(Fe) ceramics. As shown in Fig. 6 (c)-(e), the O 1s spectrum was

mainly composed of O-C, O-N and O-Si bonds, the C 1s spectrum of C-O, C-C and Si-C bonds, and the N1s spectrum of N-Si and N-O bonds [36-38]. According to the above results, the SiCN(Fe) ceramics comprised of the following phases: $SiO_xC_yN_z$, graphite, turbostratic carbon, SiC and a small amount of Fe_3Si [39,40].

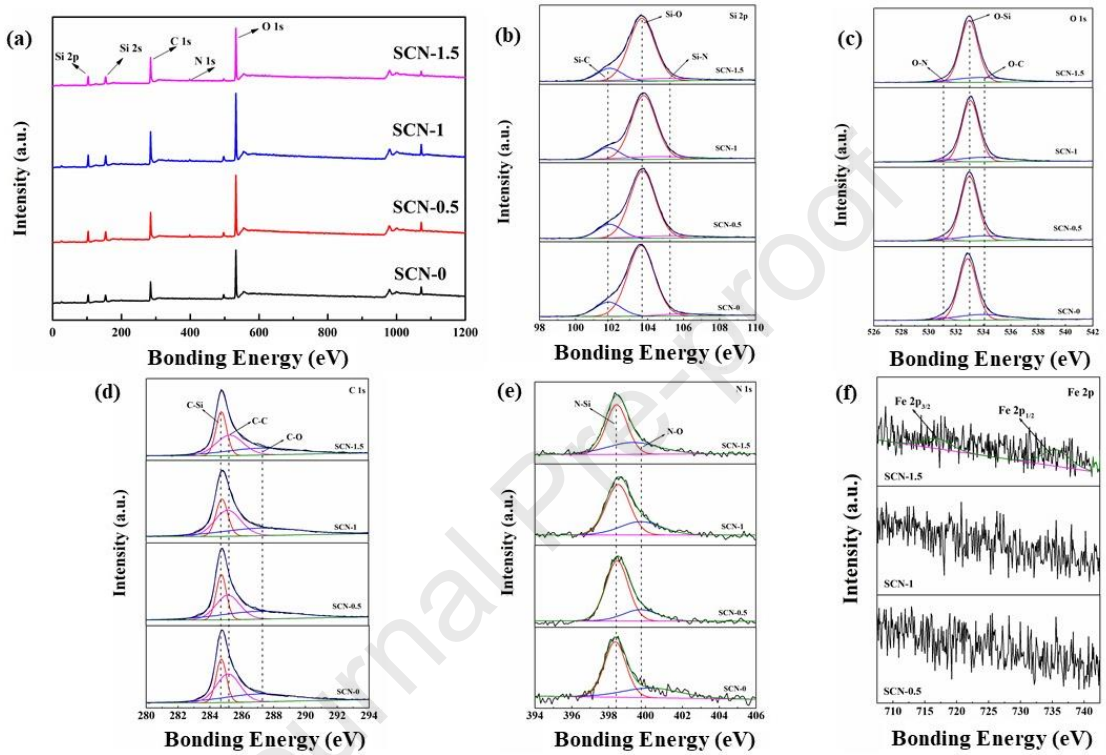

Fig. 6. XPS spectra of SiCN(Fe) samples.

(a) full spectrum; (b) Si 2p; (c) O 1s; (d) C 1s; (e) N 1s; (f) Fe 2p.

The XRF analysis (shown in Table 1) confirmed that the samples had a composition similar to the one reported by Flores et al. for the same precursor [41], with some oxygen contamination present in the bulk of the material due to the relatively long time required for printing consecutive thin layers in environmental conditions. Iron content was not reported due to the low sensitivity of the analytical technique employed.

Tab. 1. Element content obtained by XRF analysis

Element content (wt%)	Si	O	C	N
SCN-0	49	34	15	2
SCN-0.5	51	31	15	3
SCN-1	50	32	16	2
SCN-1.5	48	32	16	4

Fig. 7 reports the Raman spectra of the SiCN (Fe) samples prepared with different contents of ferrocene, showing that all the samples possessed obvious D and G peaks. The D peak was located near 1350 cm^{-1}, corresponding to disordered carbon with defects. The G peak, located near 1580 cm^{-1}, was related to the plane vibration of the sp^2 orbital of the carbon atom in the graphite (ordered) lattice, indicating the existence of both defective amorphous carbon (such as turbostratic carbon and defective graphite) and ordered crystalline graphite [42]. With the introduction of ferrocene, the (partial) overlapping of the D and G peaks decreased significantly and the half-peak width decreased gradually, indicating that the introduction of ferrocene increased the crystallization degree of free carbon in the materials. The Gauss-Lorentz fitting curves and Raman fitting parameters are shown in Fig. 7 (b)-(e) and reported in Table 2, respectively; the value of the I_D/I_G ratio reflects the degree of carbon crystallization into graphite. The results showed that the I_D/I_G ratio decreased at first and then increased after the introduction of ferrocene, indicating that the crystallization degree of the free carbon phase in the sample structure was constantly changing [43]. In agreement with TEM image analysis, we can state that the introduction of ferrocene significantly improved the degree of graphite crystallization in the samples, and also promoted the precipitation of turbostratic carbon in the

Si-C-N network structure [44]. The I_D/I_G values indicate that the amount of precipitated turbostratic carbon was much greater than the amount of formed crystalline graphite, leading to the gradual increase of the I_D/I_G ratio after adding more ferrocene. Therefore, the addition of ferrocene influences the pyrolysis and the associated crystallization behavior of the polymer precursor, leading to graphite possessing a high degree of crystallization [32].

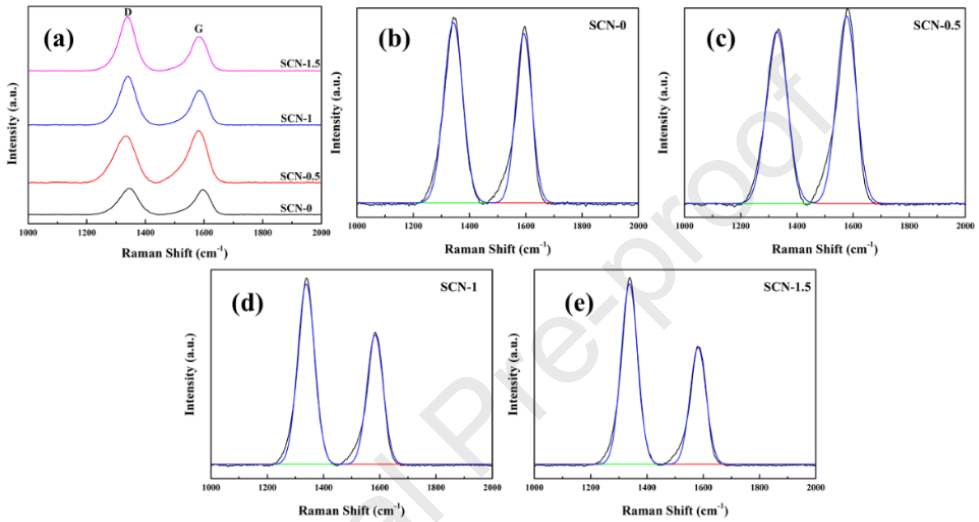

Fig. 7. Raman spectra of the SiCN(Fe) samples: (a) full spectrum; (b) SCN-0 fitting spectrum; (c) SCN-0.5 fitting spectrum; (d) SCN -1 fitting spectrum; (e) SCN-1.5 fitting spectrum.

Tab. 2. Raman fitting data of the SiCN (Fe) ceramics

Sample	W_D (cm^{-1})	F_D (cm^{-1})	W_G (cm^{-1})	F_G (cm^{-1})	I_D/I_G
SCN-0	1342.64	79.69	1593.08	67.57	1.23
SCN-0.5	1329.61	88.31	1577.05	82.34	0.99
SCN-1	1338.63	71.37	1583.06	68.26	1.41
SCN-1.5	1337.63	70.05	1582.07	67.95	1.52

Fig. 8 reports the complex permittivity ($\varepsilon_r = \varepsilon' - j\varepsilon''$) of the SiCN(Fe) ceramic powders. As shown in Fig. 8(a) and (b), the real and imaginary permittivity values of the SCN-0 sample were

relatively stable in the measurement frequency band range (2-18 GHz), and the dispersion characteristics became evident with the increase of frequency. With the addition of ferrocene, the real and imaginary permittivity values of the SiCN(Fe) ceramics were greatly increased, and the initial real permittivity went from 13 (SCN-0) to 20-23. In addition, the samples containing ferrocene displayed an obvious relaxation phenomenon at high frequency (above 12 GHz), and the loss tangent of permittivity increased significantly in the 10-18 GHz frequency range (Fig. 8(c)), indicating that this additive effectively improved the dielectric loss of the SiCN(Fe) ceramics. The carbothermal reduction reaction between ferrocene and the polymer precursor at high temperature catalyzed the decomposition of hydrocarbons to C and H_2, leading to the formation of more ordered carbon phases and SiC. Therefore, the large amount of precipitated phases can produce significant interfacial and dipole polarization, thus enhancing the dielectric loss [45]. Fig. 8(d) shows the Cole-Cole curves of the samples. The results showed that the SiCN(Fe) ceramics possessed multiple semicircles with different sizes, as a function of the composition, indicating that multiple polarization processes active in the samples [46]. Compared with SCN-0, the Debye circle of the samples containing ferrocene was closer to a perfect semi-circularity, especially for SCN-1. This might be caused by the introduction of ferrocene in the polymer precursor, which catalyzed the high crystallization degree of graphite and SiC nano-sized particles, resulting in an obvious dipole polarization effect.

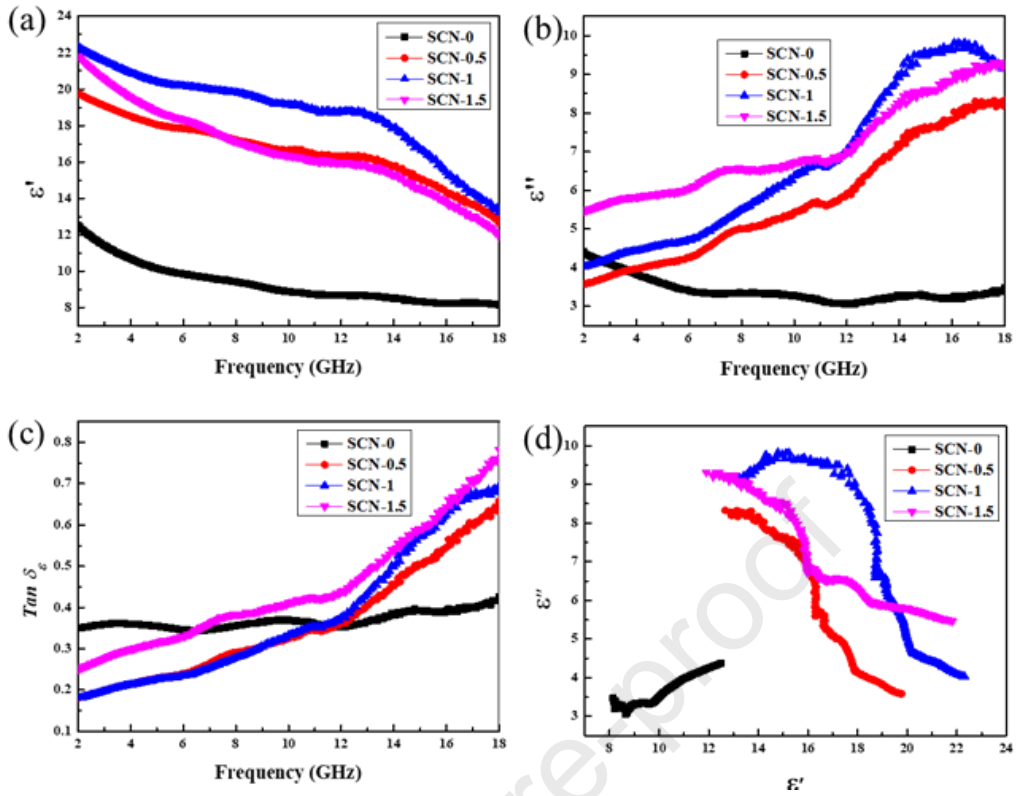

Fig. 8. (a) Real permittivity; (b) imaginary permittivity; (c) loss tangent of permittivity; (d) ε′-ε″ curve for the SiCN(Fe) ceramics.

Fig. 9 (a), (b) and (c) show that the magnetic natural resonance of the SiCN(Fe) ceramic powders obtained by introducing magnetic fillers (ferrocene) was significantly enhanced. However, due to the small amount of filler, the complex permeability parameters of the samples led to its weak contribution to the magnetic loss. In addition, the value of μ" in a specific frequency band was negative, and the tangent angle of magnetic loss was also negative. This is due to the formation of a large number of conductive nanosized phases, catalyzed by ferrocene, such as turbostratic carbon, graphite and SiC. Furthermore, the phases formed conductive channels and generated induced magnetic field under the action of alternating electromagnetic field, releasing a part of the magnetic energy [47]. However, the weak magnetic loss introduced by ferrocene was not enough to offset the magnetic energy radiation that generated inside,

which led to the negative value of μ". The magnetic loss was mainly caused by eddy current loss and ferromagnetic resonance in the range of 2-18 GHz [48,49]. When the magnetic loss is only caused by the eddy current loss, the value of $C_0 = \mu''(\mu')^{-2}f^{-1}$ does not change with the frequency. As shown in Fig. 6-9 (d), the C_0 of the samples with different ferrocene contents varied with the frequency band. With increasing the amount of ferrocene, the frequency band of the ferromagnetic resonance phenomenon increased, mainly concentrated in part of the S band (2-4 GHz) and of the X band (8-12 GHz), while it was mainly unchanged at the other frequencies, indicating that the magnetic loss of the samples was primarily due to eddy current loss, and accompanied by magnetic resonance loss in the middle and low frequencies [50,51].

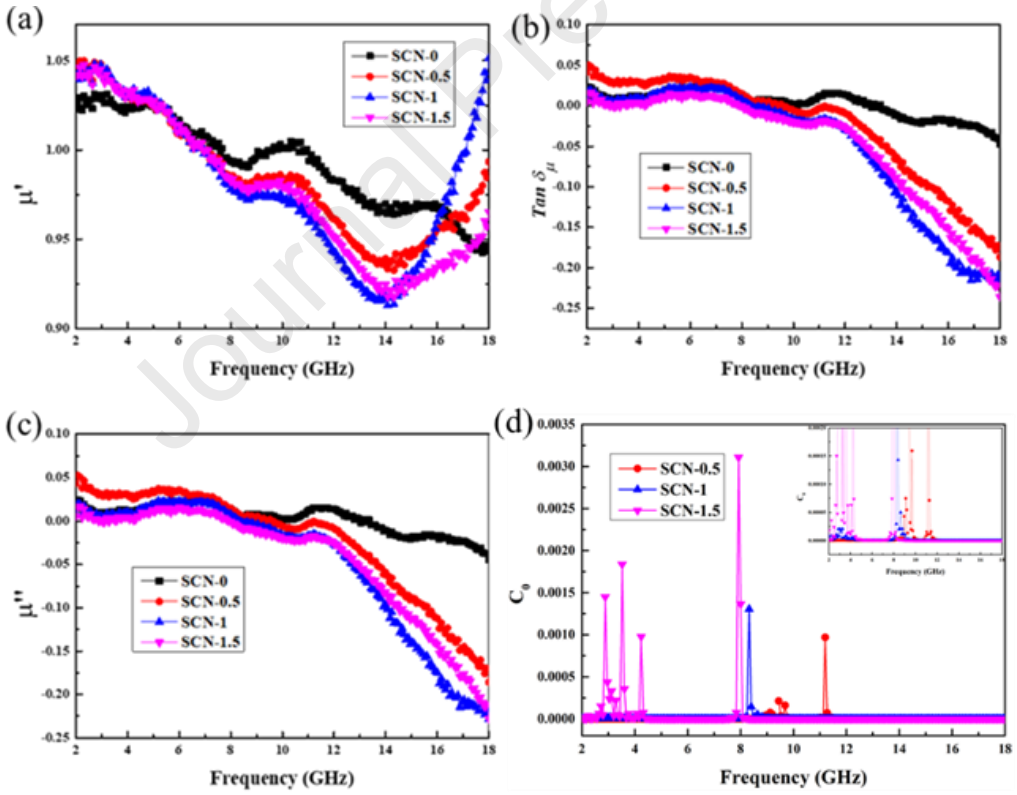

Fig. 9. (a) Real permeability; (b) imaginary permeability; (c) loss tangent of permeability; (d) magnetic loss curve for the SiCN(Fe) ceramics.

Fig. 10 shows the reflection loss of the SiCN(Fe) ceramic powders. Sample SCN-0 possessed good EMW absorption performance with a broad EAB band of 4.82 GHz (13.18-18 GHz) at the thickness of 1.81 mm, and the RL_{min} was -31.25 dB at 4.67 mm. With the addition of ferrocene, the abundant formation of nanosized phases catalyzed by ferrocene during the pyrolysis process (turbostratic carbon, graphite, SiC), providing large amounts of dipole polarization, significantly improved the EMW absorption performance of the samples. Meanwhile, the large number of heterogeneous interfaces formed when ferrocene was introduced led to the significant interfacial polarization [28]. The EAB band of SCN-0.5 was 4.57 GHz with a thin thickness of 1.30 mm, and the RL_{min} reached -61.34 dB at 2.22 mm. For SCN-1, the EAB band was 4.28 GHz at the thickness of 1.23 mm, and the RL_{min} was -50.91 dB at 2.34 mm. With the further increase of ferrocene, the RL_{min} and EAB band of SCN-1.5 decreased to -44.58 dB (4.92 mm) and 4.41 GHz (1.32 mm). Generally, a change in the reflection loss is related to a change of the internal composition of a sample. According to the previous analysis, a competition for growth between graphite and SiC crystals existed in the samples. With the increase in ferrocene, the catalytic effect changed from promoting the formation of graphite and SiC to preferentially promoting the crystallization of graphite after SiC nucleation and growth. In addition, an appropriate amount of ferrocene (0.5 wt%, for SCN-0.5) can promote the uniform precipitation of graphite, SiC and turbostratic carbon phases at the same time, maximizing the catalytic effect [52].

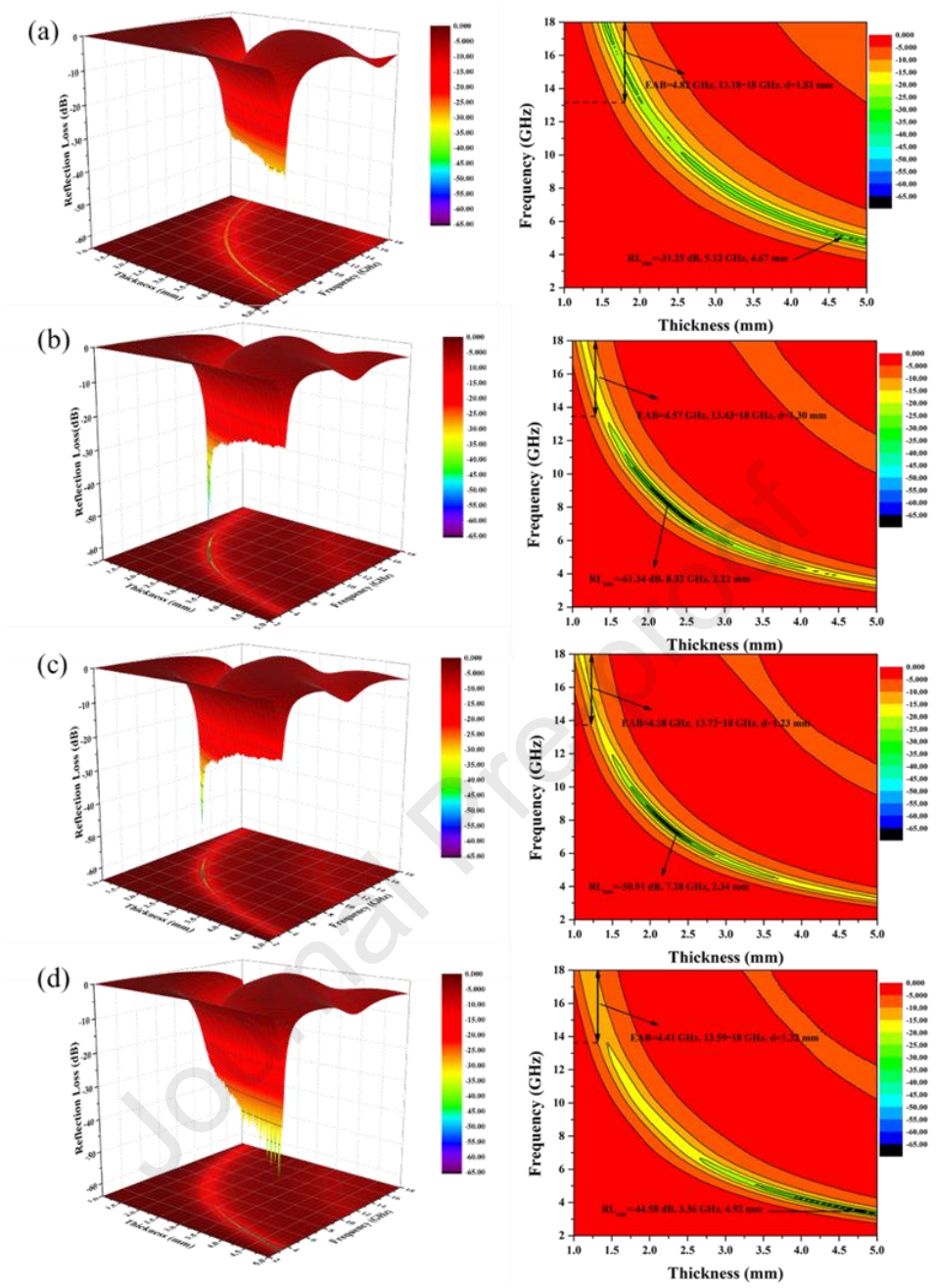

Fig. 10. Reflection Loss (RL) of the SiCN(Fe) ceramics at 2-18GHz.

(a) SCN-0; (b) SCN-0.5; (c) SCN-1; (d) SCN-1.5.

The thickness corresponding to the absorption peak calculated by the transmission line theory was compared with the equally matched thickness curve calculated by the quarter-wavelength theory. The results show that the equal-matching thickness curves of the SiCN(Fe)

ceramics intersected with the λ/4 and 3λ/4 curves (Fig 11), indicating the presence of two absorption bands in the range of 2-18 GHz, which is consistent with the absorption band in Fig 10. Meanwhile, it was also shown that the thickness corresponding to the reflection loss peak of the samples was similar to the thickness calculated by the wavelength of 1/4 and 3/4. Therefore, the SiCN(Fe) ceramics possessed phase offset under the size effect in the EMW absorption process, which indicated that interference loss and absorption loss play a synergistic role in the materials, proving also their applicability in the field of EMW absorption. Therefore, these data enable to select the thickness of SiCN(Fe) components in practical application [53].

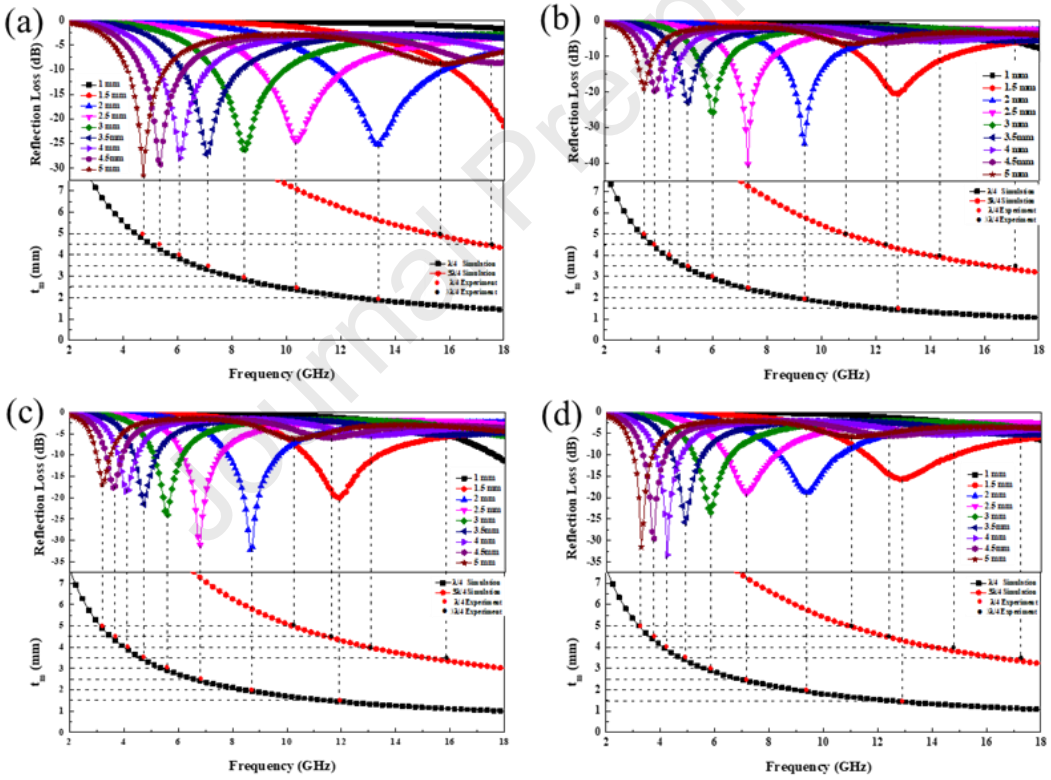

Fig. 11. Reflection loss curves and equally matched thickness curves of the SiCN(Fe) ceramics. (a) SCN-0; (b) SCN-0.5; (c) SCN-1; (d) SCN-1.5.

In order to further explore the EMW absorption mechanism of the SiCN(Fe) ceramic powders, the impedance matching diagram and attenuation constant curve were drawn to

describe the characteristics of the materials. In general, a strong electromagnetic attenuation ability and good impedance matching characteristics can promote the penetration of EMW inside a material, to obtain sufficient attenuation in its interior [54]. According to transmission line theory, when the EMW from free space impinges onto the material surface, $|Z_{in}/Z_0|$ value closer to 1 indicate that its easier for the EMW to enter the absorbing material. Meanwhile, the larger the region where Z value is close to 1, the higher impedance matching performance of the sample. As shown in Fig. 12 (a)-(d), the range of optimal impedance matching (Z=0.8-1.2) of the samples was consistent with the trend of effective reflection loss frequency band, and also highly consistent with the λ/4 curve of interference loss [55]. The optimal impedance matching range of SCN-0 was wide, indicating that the SiCN(Fe) ceramics possessed good impedance matching performance. With the increase content of ferrocene, the optimal impedance matching region of the samples gradually decreased. Due the catalytic effect of ferrocene, the preceramic polymer precursor produced at high temperature a large number of phases providing dielectric losses, which greatly improved the dipole polarization and interfacial polarization of the material, leading to a significant improvement in its dielectric properties [56]. However, the magnetic characteristics provided by the small amounts of magnetic material present were not enough to modify the dielectric properties. As a result, the EAB of the SiCN(Fe) ceramics was slightly reduced, while the RL_{min} was significantly increased. In addition, another important factor that determined the EMW absorption capacity of the samples was the electromagnetic attenuation capacity. Fig 12 (e) reports the attenuation constant (α) curves of the samples, which represented the EMW loss capacity inside the material. The results show that the EMW attenuation of the ceramics containing ferrocene was

significantly enhanced, which was consistent with the measured dielectric loss results.

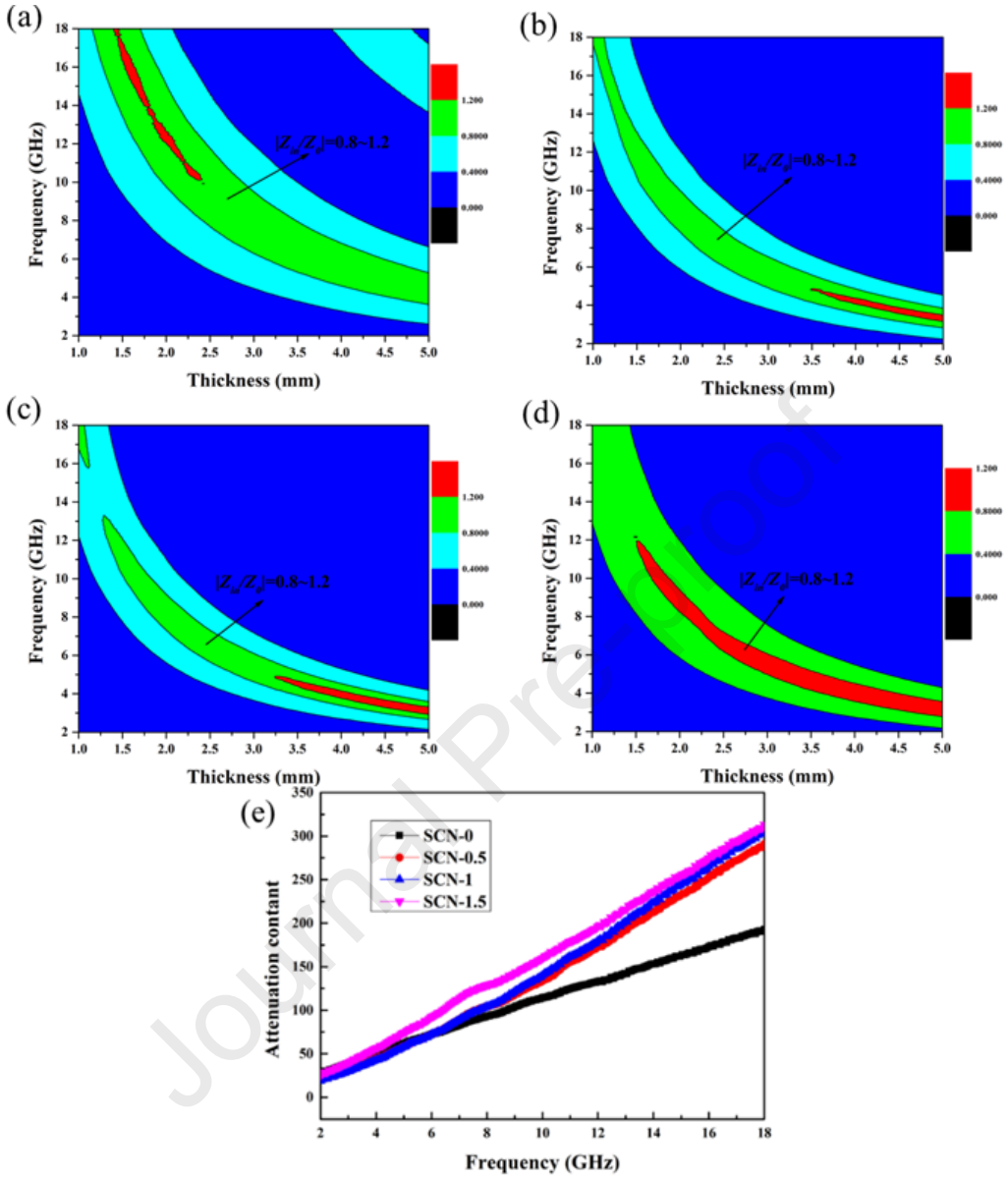

Fig. 12. Plots of $|Z_{in}/Z_0|$ of the SiCN(Fe) ceramics.

(a) SiCN-0; (b) SiCN-0.5; (c) SiCN-1; (d) SCN-1.5; (e) α.

Fig 13 shows the physical model of the EMW absorption mechanism for the SiCN(Fe) ceramics. The microstructure of the samples comprises a Si-C-N network structure embedding different nanosized phases, such as turbostratic carbon, graphite, β-SiC and a very small amount of Fe_3Si. The EMW absorption of the SiCN(Fe) ceramics was caused by the following

mechanisms: 1) the large defects in graphite, β-SiC and turbostratic carbon, which lead to dipole polarization loss; 2) the large number of heterogeneous interfaces present between the nanophases and the matrix, which induce charge accumulation, and increase the polarization loss at the interface; 3) the presence of nanosized electrically conductive graphite and β-SiC could promote the formation of charge conductive channels and increase the conductivity loss; 4) the magnetic resonance loss and eddy current loss within the material, caused by the introduction of ferrocene; 5) the diamond architecture provides several interfaces which can reflect the electromagnetic waves, and therefore is of interest for EMW absorbing components with complex structures. Therefore, under the interaction of the above loss mechanisms, the SiCN(Fe) ceramics obtained in this study appear to be promising novel structural components with good EMW absorption performance. Furthermore, it should be noticed that the phase assemblage within the ceramic can be modified by changing the heat treatment schedule, therefore providing additional freedom for obtaining enhanced characteristics.

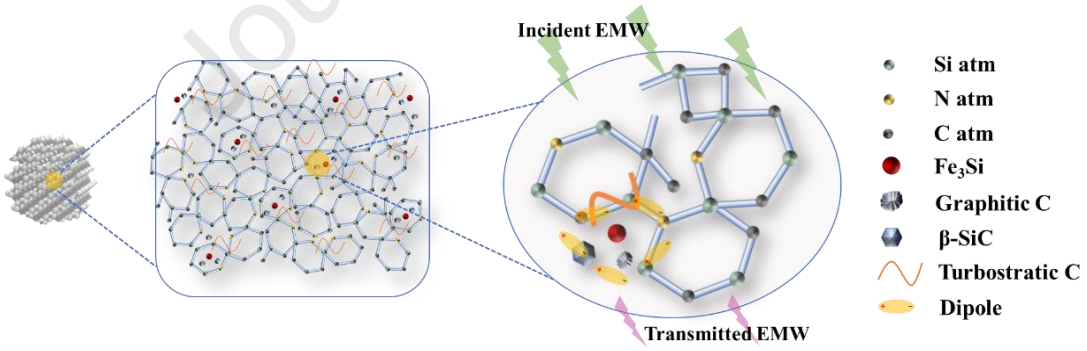

Fig. 13. Schematic diagram of possible microwave radiation absorption mechanisms in the SiCN(Fe) ceramics.

The EMW absorption performance of 3D printed ceramic blocks (with or without

ferrocene) was tested on samples obtained from the gyroid structure shown in Fig. 14. The good shape accuracy and retention after pyrolysis can be observed in both the as-printed and heat-treated sample.

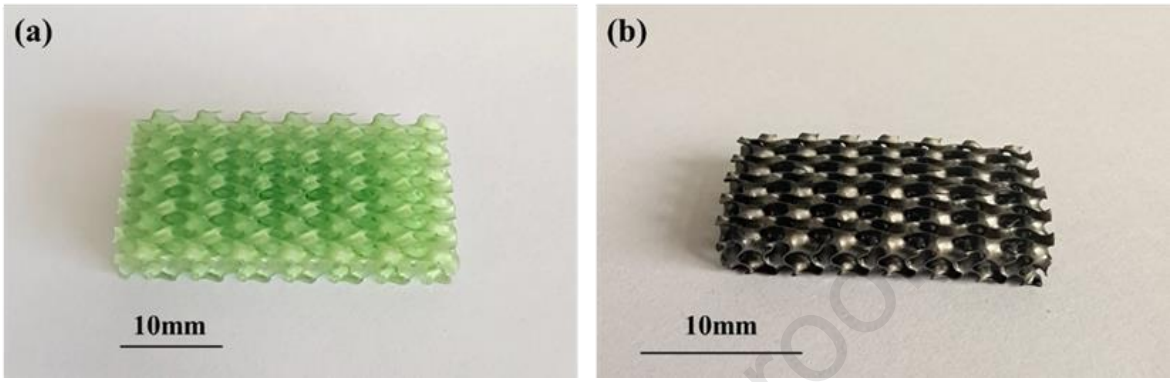

Fig. 14. 3D-SiCN-0.5 gyroid sample: (a) as printed; (b) after pyrolysis at 1200°C.

The EMW absorption performance of the 3D-printed SiCN(Fe) gyroid ceramics in the X-band, tested by waveguide method, is reported in Fig. 15. The results indicated that when the thickness of the sample was 2 mm, the reflection loss of the 3D-SiCN-0 sample was lower than -3.5 dB in the X-band (Fig. 14(a)). With the introduction of ferrocene, the EMW absorption performance was improved. The RL_{min} of the 3D-SiCN-0.5 sample was -6 dB, and the reflection loss of X-band was lower than -4 dB at 2 mm (Fig. 14(b)), which meant that more than 60.2 % of the EMW was effectively absorbed. With further increase content of ferrocene, the EMW absorption performance of the 3D-SiCN-1 sample of the same thickness decreased (Fig. 14(c)). According to the impedance matching curve, the Z_{max} value of sample SiCN-1 reached the optimal value of 0.45, indicating that the addition of ferrocene effectively improved the impedance matching characteristics of the material, increasing the EMW absorption performance of 3D-SiCN(Fe) ceramics.

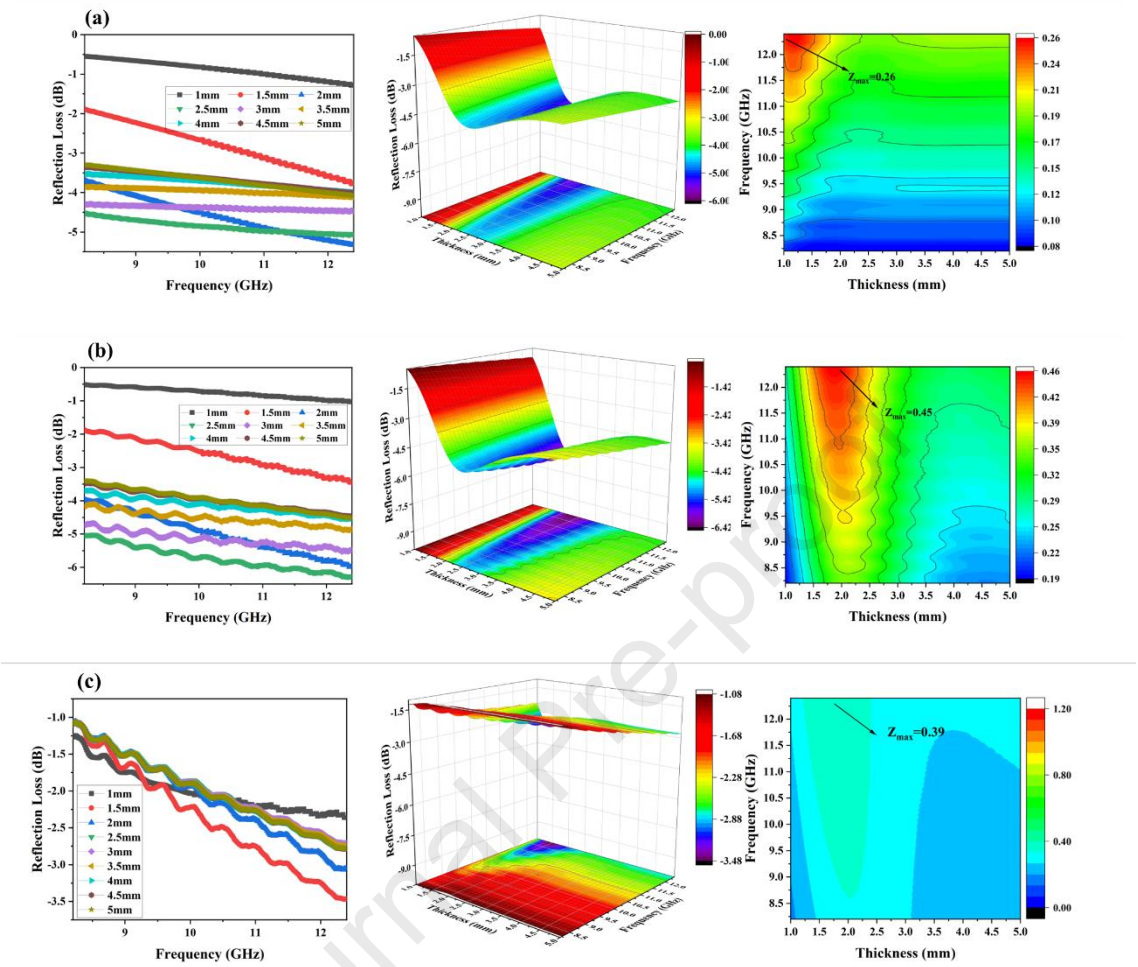

Fig. 15. Reflection Loss (RL) and $|Z_{in}/Z_0|$ of the 3D-SiCN(Fe) ceramics.

(a) 3D-SiCN-0; (b) 3D-SiCN-0.5; (c) 3D-SiCN-1

The test results for the SiCN(Fe) samples were different from those for the 3D-SiCN(Fe) samples. The former test was actually a mixture of SiCN(Fe) ceramic powder and paraffin. In the practical application, it needs to be mixed with the polymer coating with wave penetration performance, and then the mixture is coated on the surface of the material by spraying. These insulation and wave permeability of polymer coatings could effectively separate the absorbing agent, thus enhancing their impedance matching properties. During the test, the powder is

evenly dispersed in paraffin wax, which is equivalent to its practical application. Nevertheless, the 3D-SiCN(Fe) ceramics with a gyroid structure prepared in this study possessed EMW absorption properties. In further studies, the EMW absorption performance of 3D-SiCN(Fe) based structure-functional integrated ceramics will be enhanced by optimizing the structure and composition design.

4. Conclusions

The blending of silazane precursor with a commercially available, organic photocurable polymer was a suitable method for the fabrication of samples with complex architectures by DLP. SiCN(Fe) ceramics were demonstrated to possess excellent EMW absorption performance. The introduction of ferrocene led to the in-situ formation of turbostratic carbon, graphite, Fe_3Si and β-SiC nanosized phases, which formed carrier channels in the electromagnetic field and increased the conductivity loss. Meanwhile, they increased the dipole polarization, interface polarization and the dielectric properties of the material, and ultimately enhanced the EMW absorption capacity of the SiCN(Fe) ceramics. Sample SCN-0 possessed good EMW absorption performance with a wide EAB of 4.82 GHz (13.18-18 GHz) at the thickness of 1.51 mm, and RL_{min} was -31.25 dB at the thickness of 4.67 mm. The addition of ferrocene significantly improved the EMW absorption properties of the SiCN(Fe) ceramics. The EAB of SCN-0.5 was 4.57 GHz at a thin thickness of 1.30 mm, and the RL_{min} was -61.34 dB at the thickness of 2.22 mm. For sample SCN-1, the EAB was 4.28 GHz at the thickness of 1.23 mm, and the RL_{min} was -50.91 dB at the thickness of 2.34 mm, while for sample SCN-1.5, the RL_{min} and EAB band decreased to -44.58 dB (4.92 mm) and 4.41 GHz (1.32 mm). The

RL_{min} of 3D-SiCN-0.5 ceramics was -6 dB, and the reflection loss of X-band was lower than -4 dB at 2mm.

Acknowledgments

This work was supported by the Natural Science Foundation of Shandong Province (ZR2022QE024, ZR2019BEM013 and ZR2019PEM012), the Postdoctoral Research Foundation of China (2019M652441) and the China Scholarship Council (CSC grant 201806220175). YF kindly acknowledges the support of the Test Center of Shandong University of Technology and the Test Center of Shandong University.

References

[1] Zhang Y, Kong J, Gu J. New generation electromagnetic materials: harvesting instead of dissipation solo. Science Bulletin, 2022, 67 (14): 1413-1415.

[2] Lv H, Yang Z, Pan H, et al. Electromagnetic absorption materials: Current progress and new frontiers. Progress in Materials Science, 2022, 127: 100946.

[3] Wen B, Zhang J, Yang G, et al. Optimal electrical conductivity and interfacial polarization induced by loaded nanoparticles on carbon nanotubes for excellent electromagnetic wave absorption performance. Journal of Colloid and Interface Science, 2022, 626: 759-767.

[4] Mei H, Zhao X, Zhou S, et al. 3d-printed oblique honeycomb Al_2O_3/SiCw structure for electromagnetic wave absorption. Chemical Engineering Journal, 2019, 372: 940-945.

[5] Wang C, Wu S, Li Z, et al. 3D printed porous biomass-derived SiCnw/SiC composite for structure-function integrated electromagnetic absorption. Virtual and Physical

Prototyping, 2022, 17(3):718-733.

[6] Wang T, Lu X, Wang A. A review: 3D printing of microwave absorption ceramics. International Journal of Applied Ceramic Technology, 2020, 17(6).

[7] Yao L, Yang W, Zhou S, et al. Design paradigm for strong-lightweight perfect microwave absorbers: The case of 3D printed gyroid shellular SiOC-based metamaterials. Carbon, 2022, 196: 961-971.

[8] Yu S, Zeng T, Yang Y, et al. Effect of an annealing treatment on the microstructure and EMW-absorbing properties of SiC_w/Si_3N_4 ceramics fabricated by 3D printing. Ceramics International, 2023, 49:1092-1101.

[9] Duan W, Fan Z, Wang H, et al. Electromagnetic interference shielding and mechanical properties of Si_3N_4-SiOC composites fabricated by 3D-printing combined with polymer infiltration and pyrolysis. Journal of Materials Research, 2017, 32(17):1-8.

[10] You X, Dai G, Deng R, et al. Fabrication of high-performance electromagnetic wave absorbing SiC composites reinforced by 3D printed carbon-based nanonetwork with Fe_3O_4 nanoparticles. Additive Manufacturing, 2022, 55: 102855.

[11] Pan Z, Wang D, Guo X, et al. High strength and microwave-absorbing polymer-derived SiCN honeycomb ceramic prepared by 3D printing. Journal of the European Ceramic Society, 2022, 42:1322-1331.

[12] Mei H, Yang W, Zhao X, et al. In-situ growth of SiC nanowires@carbon nanotubes on 3D printed metamaterial structures to enhance electromagnetic wave absorption. Materials & Design, 2021, 197:109271.

[13] Yao L, Zhou S, Pan L, et al. Multifunctional metamaterial microwave blackbody with high-

frequency compatibility, temperature insensitivity, and structural scalability. Advanced Functional Materials, 2023, 33(5): 2209340.

[14] Mei H, Yang D, Yang W, et al. 3D-printed impedance gradient Al_2O_3 ceramic with in-situ growing needle-like SiC nanowires for electromagnetic wave absorption. Ceramics International, 2021, 47(22): 31990-31999.

[15] Yang W, Yang D, Mei H, et al. 3D printing of PDC-SiOC@SiC twins with high permittivity and electromagnetic interference shielding effectiveness. Journal of the European Ceramic Society, 2021, 41(11): 5437-5444

[16] Xiao S, Mei H, Han D, et al. 3D printed SiC nanowire reinforced composites for broadband electromagnetic absorption. Ceramics International, 2019, 45(9): 11475-11483

[17] Chaudhary R, Parameswaran C, Idrees M, et al. Additive manufacturing of polymer-derived ceramics: Materials, technologies, properties and potential applications. Progress in Materials Science, 2022, 128:100969.

[18] Feng Y, Guo X, Huang K, et al. Enhanced electromagnetic microwave absorption of SiOC ceramics targeting the integration of structure and function. Journal of the European Ceramic Society, 2021, 41(13), 6393-6904.

[19] Guo X, Feng Y, Lin X, et al. The dielectric and microwave absorption properties of polymer-derived SiCN ceramics. Journal of the European Ceramic Society, 2018, 38(4): 1327-1333.

[20] Yuan K, Han D, Liang J, et al. Microwave induced in-situ formation of SiC nanowires on SiCNO ceramic aerogels with excellent electromagnetic wave absorption performance. Journal of Advanced Ceramics, 2021, 10(5):1140-1151.

[21] Wang S, Gong H, Zhang Y, et al. Microwave absorption properties of polymer-derived SiCN(CNTs) composite ceramics. Ceramics International, 2021, 47(1): 1294-1302.

[22] Shao G, Liang J, Zhao W, et al. Co decorated polymer-derived SiCN ceramic aerogel composites with ultrabroad microwave absorption performance. Journal of Alloys and Compounds, 2020, 813: 152007.

[23] Schmalz T , Kraus T , M Günthner, et al. Catalytic formation of carbon phases in metal modified, porous polymer derived SiCN ceramics. Carbon, 2011, 49(9):3065-3072.

[24] Zaheer M , Schmalz T , Motz G , et al. Polymer derived non-oxide ceramics modified with late transition metals. Chemical Society Reviews, 2012, 41(15):5102-5116.

[25] Kong J, Schmalz T, Motz G, et al. Magnetoceramic nanocrystals from the bulk pyrolysis of novel hyperbranched polyferrocenyl(boro)carbosilanes. Journal of Materials Chemistry C, 2013, 1(7): 1507-1514.

[26] Viard A, Kurz H, Lale A, et al. Superparamagnetic Silicon Carbonitride Ceramic Fibers Through In Situ Generation of Iron Silicide Nanoparticles During Pyrolysis of an Iron-Modified Polysilazane. ACS Applied Materials & Interfaces, 2021, 13(7): 8745-8753.

[27] Ren F, Yin X, Mo R, et al. Hierarchical carbon nanowires network modified PDCs-SiCN with improved microwave absorption performance. Ceramics International, 2019, 45(11): 14238-14248.

[28] Chen Q, Li D, Liao X, et al. Polymer-Derived Lightweight SiBCN Ceramic Nanofibers with High Microwave Absorption Performance[J]. ACS Applied Materials & Interfaces, 2021, 13(29): 34889-34898.

[29] Qin H, Liu Y, Ye F, et al. Dielectric and microwave absorption properties of SiCnw-

SiBCN composite ceramics deposited via chemical vapor infiltration. Journal of Alloys and Compounds, 2019, 771: 747-754.

[30] Flores O, Schmalz T, Krenkel W, et al. Selective cross-linking of oligosilazanes to tailored meltable polysilazanes for the processing of ceramic SiCN fibres. Journal of Materials Chemistry A, 2013, 1(48): 15406-15415.

[31] Yu Y, An L, Chen Y, et al. Synthesis of SiFeC magnetoceramics from reverse polycarbosilane-based microemulsions. Journal of the American Ceramic Society, 2010, 93(10): 3324-3329.

[32] Qin H, Liu Y, Ye F, et al. Dielectric and microwave absorption properties of SiCnw-SiBCN composite ceramics deposited via chemical vapor infiltration. Journal of Alloys and Compounds, 2019, 771: 747-754.

[33] Colombo P, Mera G, Riedel R, et al. Polymer-derived ceramics: 40 years of research and innovation in advanced ceramics. Journal of the American Ceramic Society, 2010, 93(7): 1805-1837.

[34] Chen X, Su Z, Zhang L, et al. Iron nanoparticle-containing silicon carbide fibers prepared by pyrolysis of $Fe(CO)_5$-doped polycarbosilane fibers. Journal of the American Ceramic Society, 2010, 93(1): 89-95.

[35] Li Y, Hu Y, Lu Y, et al. One-dimensional SiOC/C composite nanofibers as binder-free anodes for lithium-ion batteries. Journal of Power Sources, 2014, 254: 33-38.

[36] Jiang M, Xu K, Liao N, et al. Effect of sputtering power on piezoresistivity and interfacial strength of SiCN thin films prepared by magnetic sputtering. Ceramics International, 2022, 48 (2): 2112-2117.

[37] Liu Z, Li S, Wang F, et al. Hierarchically porous $FeNi_3$@FeNi layered double hydroxide nanostructures: one-step fast electrodeposition and highly efficient electrocatalytic performances for overall water splitting, Dalton Transactions, 2021, 50: 6306-6314.

[38] Wang F, Zhang K, Zha Q, et al. Honeycomb-like Ni-Mo-S on Ni foam as superior bifunctional electrocatalyst for hydrogen evolution and urea oxidation. Journal of Alloys and Compounds, 2022, 899: 163346.

[39] Yu Y, An L, Chen Y, et al. Synthesis of SiFeC magnetoceramics from reverse polycarbosilane-based microemulsions. Journal of the American Ceramic Society, 2010, 93(10): 3324-3329.

[40] Viard A, Kurz H, Lale A, et al. Superparamagnetic silicon carbonitride ceramic fibers through in situ generation of iron silicide nanoparticles during pyrolysis of an iron-modified polysilazane. ACS Applied Materials & Interfaces, 2021, 13(7): 8745-8753.

[41] Flores O, Bordia R K, Bernard S, et al. Processing and characterization of large diameter ceramic SiCN monofilaments from commercial oligosilazanes. RSC advances, 2015, 5(129): 107001-107011.

[42] Andronenko S I, Stiharu I, Menard D, et al. EPR/FMR, FTIR, X-ray and Raman investigations of Fe-doped SiCN ceramics. Applied Magnetic Resonance, 2010, 38(4): 385-402.

[43] Li Y, Zheng Z, Reng C, et al. Preparation of Si-C-N-Fe magnetic ceramics from iron-containing polysilazane. Applied organometallic chemistry, 2003, 17(2): 120-126.

[44] Dumitru A, Stamatin I, Morozan A, et al. Si-C-N-Fe nanostuctured ceramics from inorganic polymer precursors obtained by plasma polymerization. Materials Science and Engineering: C, 2007, 27(5-8): 1331-1337.

[45] Fang H, Bai S L, Wong C P. Thermal, mechanical and dielectric properties of flexible BN foam and BN nanosheets reinforced polymer composites for electronic packaging application. Composites Part A: Applied Science and Manufacturing, 2017, 100: 71-80.

[46] Liu P, Huang Y, Zhang X. Cubic $NiFe_2O_4$ particles on graphene-polyaniline and their enhanced microwave absorption properties. Composites Science and Technology, 2015, 107: 54-60.

[47] Zuo Y, Yao Z, Lin H, et al. Synthesis and characterization of carbonyl iron@ epoxy core-shell microspheres for enhanced microwave absorption performance. Journal of Materials Science, 2019, 54(18): 11827-11840.

[48] Liu P J, Yao Z J, Ng V M H, et al. Enhanced microwave absorption properties of double-layer absorbers based on spherical NiO and $Co_{0.2}Ni_{0.4}Zn_{0.4}Fe_2O_4$ ferrite composites. Acta Metallurgica Sinica (English Letters), 2018, 31(2): 171-179.

[49] Liang M, Yu X, Shemelya C, et al. Electromagnetic materials of artificially controlled properties for 3D printing applications. 2014 IEEE Antennas and Propagation Society International Symposium (APSURSI). IEEE, 2014: 227-228.

[50] Chen H, Ran L, Wang D, et al. Metamaterial with randomized patterns for negative refraction of electromagnetic waves. Applied physics letters, 2006, 88(3): 031908.

[51] Qing Y, Min D, Zhou Y, et al. Graphene nanosheet-and flake carbonyl iron particle-filled epoxy–silicone composites as thin–thickness and wide-bandwidth microwave absorber. Carbon, 2015, 86: 98-107.

[52] Kong L, Yin X, Yuan X, et al. Electromagnetic wave absorption properties of graphene modified with carbon nanotube/poly (dimethyl siloxane) composites[J]. Carbon, 2014,

73: 185-193.

[53] Su X, Wang J, Zhang X, et al. Design of controlled-morphology $NiCo_2O_4$ with tunable and excellent microwave absorption performance. Ceramics International, 2020, 46(6): 7833-7841.

[54] Lv H, Guo Y, Wu G, et al. Interface polarization strategy to solve electromagnetic wave interference issue. ACS applied materials & interfaces, 2017, 9(6): 5660-5668.

[55] Yu J, Yu J, Ying T, et al. The design and the preparation of mesoporous Ag_3PO_4 nanorod/$SrFe_{12}O_{19}$ hexagonal nanoflake heterostructure for excellent microwave absorption. Journal of Alloys and Compounds, 2019, 775: 225-232.

[56] Zhao B, Liu J, Guo X, et al. Hierarchical porous Ni@boehmite/nickel aluminum oxide flakes with enhanced microwave absorption ability. Physical Chemistry Chemical Physics, 2017, 19(13): 9128-9.

Declaration of interests

☒ The authors declare that they have no known competing financial interests or personal relationships that could have appeared to influence the work reported in this paper.

☐The authors declare the following financial interests/personal relationships which may be considered as potential competing interests: